

Sagittarius A* near-infrared flares polarization as a probe of space-time I:

Non-rotating exotic compact objects

Nicolas Aimar^{1,2} and João Luís Rosa³, Hanna Liis Tamm³, Paulo Garcia^{1,2}

¹ CENTRA, Faculdade de Engenharia, Universidade do Porto, s/n, R. Dr. Roberto Frias, 4200-465 Porto, Portugal
e-mail: ndaimar@fe.up.pt

² CENTRA, Departamento de Física, Instituto Superior Técnico-IST, Universidade de Lisboa-UL, Avenida Rovisco Pais 1, 1049-001 Lisboa, Portugal

³ Institute of Physics, University of Tartu, W. Ostwaldi 1, 50411 Tartu, Estonia

Received month xx, 2025; accepted month xx, 2025

ABSTRACT

Context. The center of our galaxy hosts Sagittarius A*, a supermassive compact object of $\sim 4.3 \times 10^6$ solar masses, usually associated with a black hole. Nevertheless, black holes possess a central singularity, considered unphysical, and an event horizon, which leads to loss of unitarity in a quantum description of the system. To address these theoretical inconsistencies, alternative models, collectively known as exotic compact objects, have been proposed.

Aims. In this paper, we investigate the potential detectability of signatures associated with non-rotating exotic compact objects within the Sgr A* polarized flares dataset, as observed through GRAVITY and future instruments.

Methods. We examine a total of eight distinct metrics, originating from four different categories of static and spherically symmetric compact objects: Black Holes, Boson stars, Fluid spheres, and Gravastars. Our approach involves utilizing a toy model that orbits the compact object in the equatorial plane, at the Schwarzschild-Keplerian velocity. Using simulated astrometric and polarimetric data with present GRAVITY and future GRAVITY+ uncertainties, we fit the datasets across all metrics examined. We evaluated the detectability of the metric for each dataset based on the resulting χ^2_{red} and BIC-based Bayes factors.

Results. Plunge-through images of ECOs affect polarization and astrometry. With GRAVITY's present uncertainties, only a compact boson-star model is discernible. GRAVITY+'s improved sensitivity allows detection of most exotic compact object models. However, enhancing the astrophysical complexity of the hot spot model diminishes these outcomes.

Conclusions. Presently, GRAVITY's uncertainties limit us to detecting just one exotic compact object metric. With GRAVITY+'s enhanced sensitivity, we can expect to uncover additional exotic compact object models and use Sgr A* as a laboratory for fundamental physics.

Key words. Black hole physics - Relativistic processes - Polarization - Accretion, accretion disk - Radiative transfer

Use \titlerunning to supply a shorter title and/or \authorrunning to supply a shorter list of authors.

1. Introduction

The center of our galaxy hosts Sagittarius A* (Sgr A*), a supermassive compact object of $(4.297 \pm 0.012) \times 10^6$ solar masses at a distance of only $8,277 \pm 9$ pc (GRAVITY Collaboration et al. 2022; Gravity Collaboration et al. 2023). It is surrounded by star clusters, e.g. the so-called S-Star cluster, in which stars orbit around the compact object. The S-star proximity to Sgr A* and their orbital parameters allowed to test General Relativity for supermassive compact objects, like the gravitational redshift for the star S2 (GRAVITY Collaboration et al. 2018a) or the Schwarzschild precession (GRAVITY Collaboration et al. 2020). The orbit of these stars has been used to constrain the enclosed extended mass within the apocenter of S2 to be $\leq 3000 M_{\odot}$, that is, $\leq 0.1\%$ of the mass of the supermassive compact object (GRAVITY Collaboration et al. 2022). The S2 orbit has also been used to constrain the presence of scalar clouds (Foschi et al. 2023), vector clouds (GRAVITY Collaboration et al. 2024) and a fifth force (The GRAVITY Collaboration et al. 2025) around Sgr A* without any significant evidence of their presence for

scalar and vector clouds and with upper limits for the fifth force. Indeed, the closest pericenter passage of the stars detected so far is still at a few thousand gravitational radii r_g , i.e. not in the strongest gravitational regime. The current observational state-of-the-art cannot fully constrain the nature of the supermassive compact object at the center of the galaxy. (De Laurentis et al. 2023).

The Event Horizon Telescope (EHT) has provided the first horizon-scale image of Sagittarius A* (Sgr A*), the supermassive object at the center of our galaxy (Event Horizon Telescope Collaboration et al. 2022). This landmark observation opens the door to testing the nature of compact objects in the strong gravity regime. While the image is broadly consistent with the predictions of general relativity for a Kerr black hole, it does not definitively rule out the existence of exotic compact objects (ECOs) that mimic many black hole features but lack an event horizon (Carballo-Rubio et al. 2022; Vagnozzi et al. 2022; Shaikh 2022). Current resolution and modeling uncertainties allow for a range of ECO models—such as boson stars, gravastars, or worm-

holes—to remain compatible with the EHT data (Doe & Others 2024).

Since 2001, outbursts of radiation called flares have been detected from Sgr A* in X-rays (Baganoff et al. 2001; Nowak et al. 2012; Neilsen et al. 2013; Barrière et al. 2014; Ponti et al. 2015; Haggard et al. 2019), near-infrared (NIR; Genzel et al. 2003; Ghez et al. 2004; Hornstein et al. 2007; Hora et al. 2014) and radio (Yusef-Zadeh et al. 2006; Bower et al. 2015; Brinkerink et al. 2015). In the past two decades, Sgr A* flares have been the subject of intense observational campaigns and research, although no consensus has yet been reached on their physical origin. Indeed, multiple types of models exist for Sgr A* flares including (among others) red noise (Do et al. 2009), hot-spot (Genzel et al. 2003; Broderick & Loeb 2006; Hamaus et al. 2009), ejected blob (Vincent et al. 2014), star-disk interaction (Nayakshin et al. 2004), disk instability (Tagger & Melia 2006), or magnetic reconnection (Aimar et al. 2023; Lin et al. 2023).

Thanks to interferometric measurements with the GRAVITY/VLTI instrument (GRAVITY Collaboration et al. 2017), the GRAVITY Collaboration reported the detection of orbital motion for Sgr A* flares (GRAVITY Collaboration et al. 2018b; Gravity Collaboration et al. 2023) at ~ 9 gravitational radii (r_g) with a low inclination $i \sim 160^\circ$ compatible with the constraints from the Event Horizon Telescope Collaboration et al. (2024) results of $i \approx 150^\circ$. This detection brought important constraints on Sgr A* flares modeling, favoring hot-spot and ejected blob models. However, the physical origin of Sgr A* flares is still under debate.

Flares occur at only a few gravitational radii in the strong-field regime. They are thus an ideal object to study and constrain the space-time, and so the nature of Sgr A* (Schwarzschild, Kerr, or non-Kerr). Although the effects of spin or Exotic Compact Object metrics (non-Kerr metrics) on the flare light curves are too small to be detected or degenerate with model parameters, the measure of the astrometry of flares with GRAVITY was thought to be sufficient to detect the non-Kerr metric signature. However, the low inclination and large uncertainties in the astrometric data do not allow such a detection (Li et al. 2014; Li & Bambi 2014; Liu et al. 2015; Rosa et al. 2023).

The detection of polarization of Sgr A* flares in NIR (GRAVITY Collaboration et al. 2018b; Gravity Collaboration et al. 2023) and in radio (Wielgus et al. 2022) brought new observational constraints on the magnetic field configuration. In both wavelengths, the observed polarization properties (QU loops and angular polarization velocity) are only compatible with a vertical magnetic field. Vincent et al. (2024) showed that the observed loop(s) in the QU plane are mainly due to the special relativity of the orbital motion of the emitting region. However, General Relativity, mainly light bending, also affects the observed QU loop(s) creating an asymmetry relative to the horizontal axis (Vincent et al. 2024). **In other words, linear polarization measured with Stokes parameters is sensitive to space-time curvature and therefore can constrain the nature of Sgr A*.**

Although the space-time around black holes can effectively describe the observations mentioned in the foregoing sections, these space-times present inherent difficulties from both mathematical and physical viewpoints. In essence, black hole space-times are characterized by singularities Penrose (1965, 1969), hinting at potential incompleteness within the theoretical framework. Moreover, the presence of an event horizon in black hole physics leads to the so-called black hole information paradox, in which the thermal nature of Hawking radiation implies a potential loss of information. This contradicts the principle of unitary evolution in quantum mechanics, where information must

be preserved over time. This tension between general relativity and quantum theory has been widely discussed since Hawking’s seminal work Hawking (1976). To remedy such challenges, a number of alternative theoretical models, collectively termed exotic compact objects (ECOs), have been proposed (see Ref. Cardoso & Pani (2019) for a review). A subset of these ECO models can emulate similar observational predictions, thereby earning the designation of black hole mimickers.

The primary objective of this paper is to investigate the potential detectability of signatures associated with non-rotating ECOs within the Sgr A* polarized flares dataset, as observed through the GRAVITY instrument. In Sect. 2, we discuss the various ECOs metric models that were taken into consideration for this study, while Sect. 3 elaborates on the flare model itself. The methodological framework is delineated in Sect. 4, followed by the presentation of our findings in Sect. 5. We discussed our results in Sect 6 and made a summary accompanied by the conclusion in Sect. 7.

2. Horizonless Exotic Compact Objects metrics

We analyze three types of static and spherically symmetric exotic compact objects whose optical properties have been previously analyzed with GYOTO in the context of infrared flares and radio (EHT) imaging. These are the solitonic Boson star (Rosa et al. 2022; Rosa et al. 2023), the relativistic perfect-fluid sphere (Tamm & Rosa 2024), and the gravitational vacuum star (Gravastar) (Rosa et al. 2024). All the selected models have a shadow that mimics the one of a black hole and are compatible with EHT observations. More information about these models can be found in the references above. In the following, for self-consistency, we summarize the fundamentals of each of these models.

2.1. Solitonic Boson star

Scalar Boson stars consist of localized solutions of self-gravitating scalar fields. They are found as solutions of the Einstein-Klein-Gordon theory described by the action

$$S = \int \sqrt{-g} \left[\frac{R}{16\pi} - \frac{1}{2} \partial_\mu \phi^* \partial^\mu \phi - \frac{1}{2} V(|\phi|^2) \right] d^4x, \quad (1)$$

where R is the Ricci scalar, g is the determinant of the metric $g_{\mu\nu}$, ϕ is the complex scalar field, with $*$ denoting complex conjugation and $|\phi|^2 = \phi^* \phi$, and V is the scalar potential. Different Boson star models are obtained depending on the form of the potential V . In particular, solitonic Boson stars are described by a potential of the form $V = \mu^2 |\phi|^2 (1 - |\phi|^2/\alpha^2)^2$, where μ is a constant that plays the role of the mass of ϕ and α is a constant free parameter of the model (see Rosa et al. 2023, 2025, for more details). The main interest behind solitonic Boson stars lies in the fact that these can be compact enough to develop bound-photon orbits while maintaining their stability against radial perturbations.

Due to the complexity of the Einstein-Klein-Gordon system of field equations, no analytical solutions describing Boson stars have been obtained. We consider two numerical solutions of solitonic Boson stars with different compacticities, a model close to the ultra-compact regime (BS2), and an ultra-compact model (BS3) described in detail in Rosa et al. (2023). Time integrated images of an orbiting hot spot around these two configurations are show in Fig. 1. We exclude the dilute model (BS1) as the observed Q-U loops for this model are large (Rosa et al. 2025)

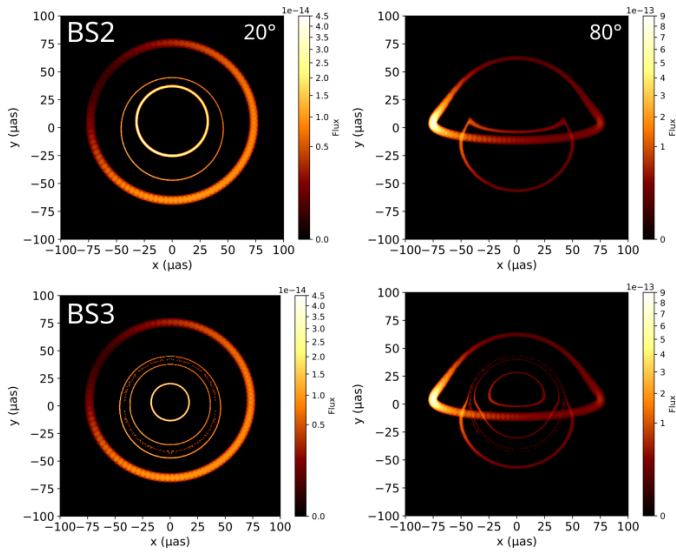


Fig. 1. Time integrated image of a hot spot orbiting the Boson star 2 model in the left column and the Boson star 3 model in the right column, close de face-on (20°) top row and close to edge-on (80°) bottom row. Extracted from Rosa *et al.* (2025).

which is incompatible with the GRAVITY data (Gravity Collaboration *et al.* 2023).

2.2. Relativistic Fluid sphere

Relativistic Fluid spheres are solutions to Einstein's field equations in the presence of an isotropic perfect fluid. The interior of these solutions is described in the usual spherical coordinates (t, r, θ, ϕ) by the metric

$$ds^2 = -\frac{1}{4} \left(3 \sqrt{1 - \frac{2M}{R}} - \sqrt{1 - \frac{2r^2M}{R^3}} \right)^2 dt^2 + \left(1 - \frac{2r^2M}{R^3} \right)^{-1} dr^2 + r^2 (d\theta^2 + \sin^2 \theta d\phi^2), \quad (2)$$

where M and R are constants that represent the mass and the surface radius of the star, respectively. The exterior of these solutions is described by the Schwarzschild solution. We restrict our analysis to smooth solutions, that is, the surface of the star R coincides with the radius at which the matching between the interior and exterior solutions is performed, and with a constant volumetric energy density. Under these restrictions, these solutions develop a pair of bound-photon orbits whenever $R \leq 3M$, with the limiting case $R = 3M$ corresponding to a single degenerate bound-photon orbit, whereas a singularity is present whenever $R \leq 2.25M$. More details about this model can be found in Ref. Tamm & Rosa (2024). Three models were studied in Tamm & Rosa (2024) with $R = 2.25M$ (FS1), $R = 2.5M$ (FS2), and $R = 3M$ (FS3), however, at low inclination (which is likely the case for Sgr A*), the FS1 model presents the same observational features as Schwarzschild. Thus, in this study, we consider only the FS2 and FS3 models. Similarly to the Boson star case, Fig. 2 shows the time integrated images of a hot spot orbiting the FS2 (top row) and FS3 (bottom row) models with low inclination (left column) and high inclination (right column).

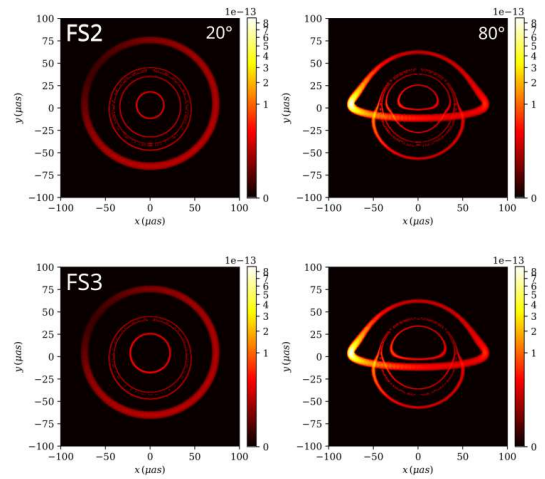


Fig. 2. Time integrated image of a hot spot orbiting the Fluid sphere 2 model in the top row and the Boson star 3 model in the bottom row, close de face-on (20°) left column and close to edge-on (80°) right column. Extracted from (Tamm *et al.*, in prep). The color bar corresponds to the total intensity in SI units.

2.3. Gravastar

Similarly to relativistic Fluid spheres, gravitational vacuum stars, or Gravastars, are solutions of the Einstein's field equations in the presence of an isotropic perfect fluid. In the case of Gravastars, this fluid is exotic, satisfying an equation of state of the form $p = -\rho$, where p is the isotropic pressure and ρ is the energy density. The interior of Gravastars is described by the metric

$$ds^2 = -\alpha \left(1 - \frac{2m(r)}{r} \right) dt^2 + \left(1 - \frac{2m(r)}{r} \right)^{-1} dr^2 + r^2 (d\theta^2 + \sin^2 \theta d\phi^2), \quad (3)$$

where α is a parameter controlling the volumetric mass distribution of the star, and $m(r) = \frac{4}{3}\pi r^3$ is the mass function. The exterior of the Gravastar is described by the Schwarzschild space-time. The parameter α is bounded between 1 and a minimum value α_{\min} that depends on the model, with $\alpha = 1$ and $\alpha = \alpha_{\min}$ corresponding to solutions with all mass distributed in volume or on the surface, respectively. Regardless of the mass distribution, these solutions develop a pair of bound-photon orbits whenever the radius R of the surface of the Gravastar, where the matching between the interior and exterior space-times is performed, satisfies the condition $R \leq 3M$, with the limiting case $R = 3M$ corresponding to a single degenerate bound-photon orbit. More details about this model can be found in Ref. Rosa *et al.* (2024). For $\alpha \neq 1$, the g_{rr} coefficient of the metric is discontinuous, making the parallel transport of the polarization basis inside the ray tracing code GYOTO (more details in Section 3.1) impossible. We thus fixed $\alpha = 1$ and selected three configurations: a model with $R = 3M$ (GS1), $R = 2.5M$ (GS2) and $R = 2.01M$ (GS3). Again, we present the time integrated images of a hotspot orbiting these three configurations in Fig. 3.

3. Hot spot model

We consider an analytical orbiting hot spot model for the flares of Sgr A* in NIR as it is the model that agrees the most with the current data. However, we did not choose any specific physical phenomenon at the origin of the flare to be not model dependent.

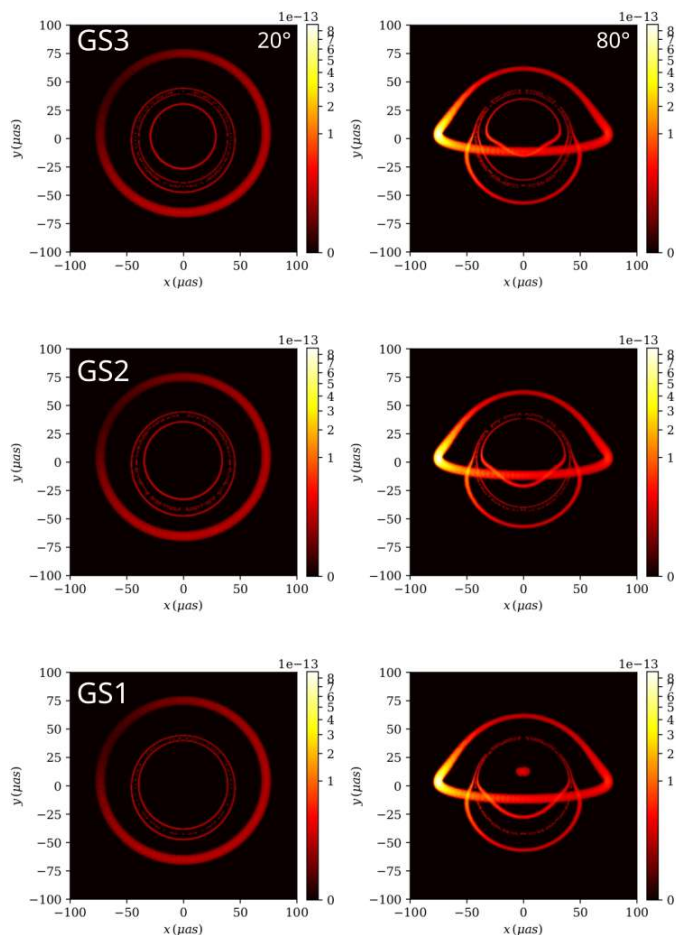


Fig. 3. Same as Fig. 2 with the Gravastar models with $R = 2.01M$ in the top row, $R = 2.5M$ in the middle row and $r = 3M$ in the bottom row. Extracted from (Tamm *et al.*, in prep).

The hot spot is assumed to be a uniform sphere of plasma with a radius of $1 r_g$ that emits synchrotron radiation.

As previously demonstrated (Li *et al.* 2014; Liu *et al.* 2015; Rosa *et al.* 2023) and depicted in Fig. 4, the current uncertainties in astrometry, alongside the fact that the flares from Sgr A* are observed nearly face-on, prevent the differentiation between various ECO and Schwarzschild models, emphasizing the necessity for polarization measurements.

3.1. Polarized ray-tracing

We used the public polarized ray-tracing code GYOTO¹ (Vincent *et al.* 2011; Aimar *et al.* 2024) to compute the images of the hot spot model for the four Stokes parameters (I, Q, U and V) which characterize the total received intensity (Stokes I) and the polarization of the received light (Q and U for linear polarization and V for circular polarization). For this study, we ignored the circular polarization V as it is not measurable by GRAVITY.

For each observing time, we compute the field integrated polarized fluxes $F_I(t)$, $F_Q(t)$, and $F_U(t)$ in Jansky, and the centroid position of the total flux $(X(t), Y(t))$ from the computed images. While polarization strongly depends on the orbital parameters and the inclination (see below), the incorporation of the astrometry allows breaking some degeneracies. For the rest of the pa-

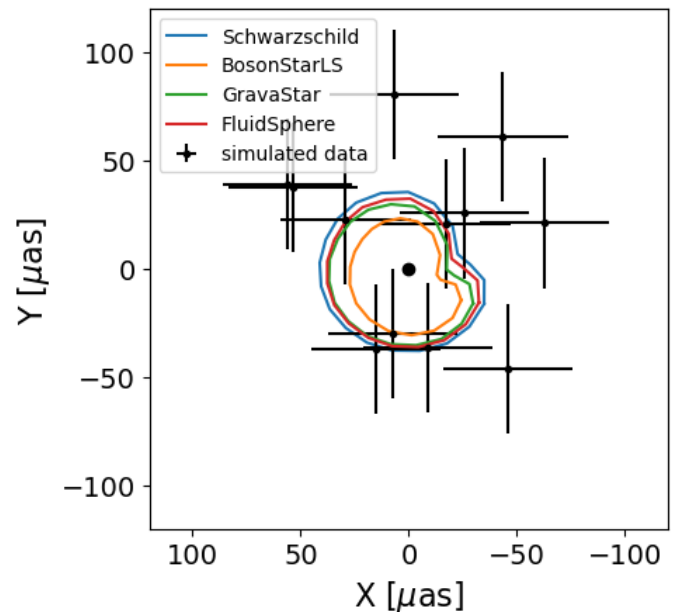


Fig. 4. Astrometry of an orbiting hot spot in different metric models and simulated astrometric data with current GRAVITY uncertainties.

per, the field of view is set to 2.6 times the orbital radius in M units to optimize the computation time, and the default resolution is 300×300 pixels. Such resolution is sufficient to get the low-order plunge-through images from the ECO models but not the high-order ones, which require an extreme resolution but have a minor impact on the observed fluxes. The differences with the Schwarzschild metric come mainly from the additional or absence of light rings and additional plunge-through images (Rosa *et al.* 2025, Tamm *et al.*, in prep). The observed wavelength is set to the one of GRAVITY, that is, $2.2 \mu\text{m}$.

3.2. Orbital motion

For this theoretical study, we choose the simplest type of orbital motion, i.e., a circular orbit at radius r in the equatorial plane with the Schwarzschild keplerian velocity, i.e., in Boyer-Lindquist coordinates,

$$\theta = \frac{\pi}{2} \quad (4)$$

$$\frac{dr}{dt} = \frac{d\theta}{dt} = 0 \quad (5)$$

$$\frac{d\varphi}{dt} = r^{-3/2}. \quad (6)$$

Note that in the ECO metrics, this choice of velocity does not necessarily correspond to time-like geodesics, nor to the Keplerian velocity in these metrics. However, this study is focused on the detectability of the effect of alternative metrics on the polarization signals. Thus, to make a proper comparison, the 3D-velocity must be the same in all metrics. Nevertheless, this assumption does not change our conclusions, as the change in velocity is negligible for non-rotating ECOs compared to the typical error bars of the problem. Furthermore, for orbital radius larger than the size of the Boson star, which is the case here, the difference of velocity between the Boson star metric and Schwarzschild is very small and can be neglected. For Gravastars and Fluid spheres, the velocity is identical to Schwarzschild outside the compact object radius.

¹ <https://github.com/gyoto/Gyoto>

3.3. Electron Energy Distribution function

The IR flux from Sgr A* flares is thought to be generated by synchrotron radiation from a non-thermal population of electrons (GRAVITY Collaboration et al. 2021). We thus consider a κ -distribution of electrons (Marszewski et al. 2021) for our hot spot. This distribution is characterized by a thermal core with a temperature T_e and a power-law tail with κ -index² and a number density n_e . These three parameters have a strong influence on the fluxes, while the κ -index governs the NIR spectral index. To simplify and limit the number of parameters, we set the number density to $5 \times 10^6 \text{ cm}^{-3}$, the temperature to $5 \times 10^{10} \text{ K}$ and the κ -index to 3.5. The overall flux of the generated synthetic flares with these settings matches the usual observed flux from Sgr A* flares ($\approx 10 \text{ mJy}$). Obviously, not all flares have the same maximum flux. To mitigate this, we restricted the study to the normalized polarized fluxes Q/I and U/I .

3.4. Magnetic field configuration

The average of polarization measurements of multiple flares made in Gravity Collaboration et al. (2023) has shown that the magnetic field configuration in the flare emitting region is vertical. Indeed, the polarization angular velocity of $\sim 6^\circ/\text{min}$ is only compatible with the vertical configuration of the magnetic field lines at low inclination. This statement remains true even in the ECOs metrics (Rosa et al. 2025, Tamm et al., in prep). We thus restrict our study to this magnetic field configuration. The magnetic field strength is defined through the magnetization parameter $\sigma = B^2/4\pi m_p c^2 n_e$ fixed to 0.01. The magnetic field strength is thus around 30 G which is the expected order of magnitude for Sgr A* flares (von Fellenberg et al. 2025). Note that in this model, this parameter is only a scaling factor of the total flux.

The observed linear polarization fraction of Sgr A* flares is $\sim 20 - 25\%$, much lower than the linear polarization fraction expected from a purely ordered magnetic field. A probable explanation is that the magnetic field is only partially ordered (Event Horizon Telescope Collaboration et al. 2024). The contribution of plunge-through images can also result in a decrease of the linear polarization fraction, but only for a part of the orbit and cannot be responsible for the global difference of polarization fraction. To take into account that the magnetic field is only partially ordered, we apply a constant scaling factor lp to the polarized quantities (Stokes Q and U), whose value is in $[0,1]$ ³.

Our model thus has a total of five parameters, summarized in Tab. 1, four for the hot spot: orbital inclination i , radius r , initial azimuthal angle φ_0 and the polarization factor lp and one for the metric (metric model). We fixed the Position Angle of the Line of Nodes to 177.3° following Gravity Collaboration et al. (2023) as this parameter add an unnecessary degree of freedom for this theoretical study.

4. Methodology

To determine the detectability of the metrics considered in this paper, we performed fits of simulated data with all the metric and compared the results of these fits. Using statistical criteria, we conclude on the detectability of the metrics. The following section describes in detail our methodology.

² related to the power law index p as $\kappa = p + 1$

³ This parameter should not be interpreted as the degree of order of the magnetic field as the relation is indirect and non-trivial.

Parameter	Symbol	Default value
Orbital radius [r_g]	r	8.2
Azimuthal angle at $t^{BL} = 0$ [$^\circ$]	φ_0	15
Inclination [$^\circ$]	i	157
Linear polarization factor	lp	0.4

Table 1. Summary of the parameters of the hot-spot model.

4.1. Generation of simulated data

We generated simulated data following the set of parameters presented in Tab. 1 for the hot spot in each ECO model metric.

In order to accommodate the uncertainties inherent in observational data, we introduce a random variable to the simulated data points, which is drawn from a Gaussian distribution. For the simulated data on astrometric measurements, the Gaussian distribution is characterized by a standard deviation denoted $\sigma_{\text{Astro}} = 30 \mu\text{as}$. Similarly, for the simulated polarized flux measurements (I, Q and U), the standard deviation is represented by σ_{Flux} . Sect. 5 provides different uncertainty values σ_i , aligning with GRAVITY's actual uncertainties ($\sigma_{\text{Flux}} = 0.2 \text{ mJy}$) and the improved precisions anticipated for GRAVITY+ upgrade ($\sigma_{\text{Flux}} = 0.03 \text{ mJy}$).

The observational duration and data point intervals are by default calibrated to resemble those of GRAVITY, namely, one measurement every 5 minutes resulting in a total of 12 observations (amounting to 60 minutes overall). In Sect. 5, we also investigated the impact of a better time sampling on the detectability of the metrics.

4.2. Fitting

4.2.1. Fitting procedure

Contrary to the four hot spot parameters, the metric parameter is not continuous (a range of values) but is instead a choice of configuration. The treatment of this parameter is thus different from the others. As part of our fit strategy, we opted to individually fit the four remaining parameters of our model, namely, the inclination, the orbital radius, the initial azimuthal angle and the polarization factor, within the context of all possible ECO + Schwarzschild background metrics. Subsequently, we conducted a comparative analysis of the results obtained.

We perform the fits in two distinct steps: 1) a grid, 2) a follow-up of the χ^2 gradient with fixed steps. For each background metric, we computed a grid of modeled data varying the orbital radius, the inclination, and the initial azimuthal angle. The linear polarization fraction is a simple scaling factor and can thus be applied as post-processing and does not require the use of GYOTO. The minimum and maximum values as the number of grid points of each parameter (including the linear polarization factor) are listed in Tab. 2. For each point on the grid, the modeled observable quantities ($Q/I(t)$, $U/I(t)$, $X(t)$, $Y(t)$) are estimated from the simulated model using linear interpolation. We evaluate the χ_{red}^2 as

$$\chi_{\text{red}}^2 = \frac{1}{\text{dof}} \sum_i \left(\frac{x_i - \mu_i}{\sigma_i} \right)^2, \quad (7)$$

where $\text{dof} = N - n$ is the number of degrees of freedom, N being the number of data points and n the number of free parameters, x_i the data point i , μ_i the model and σ_i the uncertainty of data

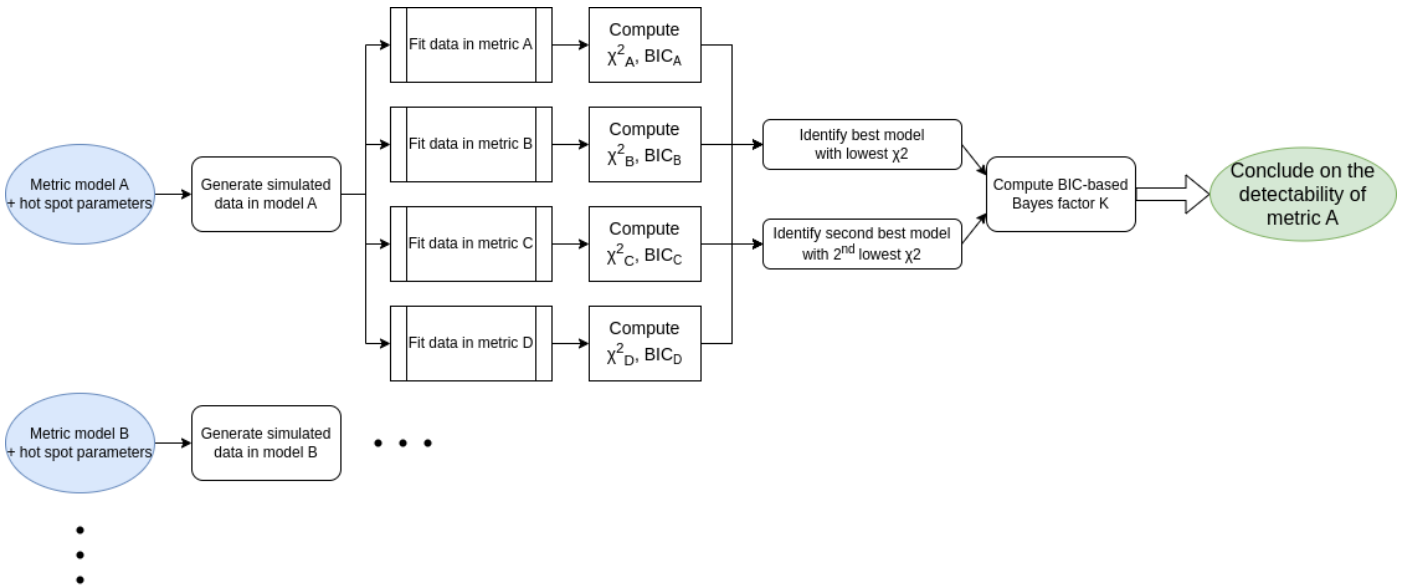


Fig. 5. Sketch illustrating our methodology to assess the detectability of ECO’s models.

point i . The grid point with minimal χ_{red}^2 is then utilized as first-guess for the `scipy.least_square` algorithm, which also use `GYOTO` to compute the model.

The approach described here enables the achievement of small error bars, without the need for an extensive grid. This is advantageous, as such a grid would be computationally demanding to produce (one per background metric).

Parameter	Range	# of grid points
Inclination [°]	[135, 170]	8
Orbital radius [r_g]	[8, 12]	9
Initial Azimuthal angle [°]	[0, 345]	24
Linear polarization factor	[0, 1]	11

Table 2. Summary of the modeled grid used for the first step of fitting.

4.2.2. Statistical criteria

We perform the fits, following the previous procedure, with all background metrics. We compute the *Bayesian Information Criterion* (BIC) to obtain the statistical criteria of the different fits. The best-fitted metric corresponds to the fit with the lowest χ_{red}^2 . We also extract the second best-fitted metric which correspond to the fit with the second lowest χ_{red}^2 . To compare these two fits and to quantify how much the best one (lowest χ_{red}^2) metric is better compared to the other, i.e. its detectability, we compute the BIC-based Bayes factor K as (Wagenmakers 2007)

$$\log_{10} K = \log_{10} \left[\exp \left(\frac{\Delta BIC}{2} \right) \right]. \quad (8)$$

As the impact of the plunge-through images (induced by the background metrics) may not be large enough to result in a significant better fit, in terms of χ_{red}^2 , for one metric compared to the others, we thus define three detectability outcomes according to the value of $\log_{10} K$ and following the Kass & and (1995) scale:

- **not detectable** : $\log_{10} K < 1$. The models are equivalent (symbolized by \times).

- **partially detectable** : $1 \leq \log_{10} K \leq 2$. In this case, the model with the lowest χ_{red}^2 is significantly better, but not enough to make a strong statement (symbolized by \sim).
- **detectable** : $\log_{10} K > 2$. The model with the lowest χ_{red}^2 is considerably better (symbolized by \checkmark).

A sketch summarizing the whole procedure is shown in Fig. 5.

5. Results

5.1. Current GRAVITY uncertainties

We first tested the detectability of the studied ECO metrics with current GRAVITY uncertainties. We generated simulated data with $\sigma_{\text{Astro}} = 30 \mu\text{as}$ and $\sigma_{\text{Flux}} = 0.2 \text{ mJy}$ in all previously listed background metrics. The flux uncertainty has been derived from the error bars in Gravity Collaboration et al. (2023) and the dereddened flux of S2 computed from Gillessen et al. (2017). We note that the flux uncertainties from interferometry depends on the sources present in the field of view, and are thus not fixed from one observation period to another. However, this value is still representative of the typical flares flux uncertainties.

For each of the generated dataset, we performed a fit in all background metrics, whose results are listed in Table 3. This table shows for each simulated data generated in a given background metric (each line), the best-fitted metric in the second column, the associated χ_{red}^2 and BIC in the third and fourth columns, respectively. We recall that we fit all the parameters of Table 1 and not only the metric. Columns five and six show the second best-fitted metric and the BIC-based Bayes factor between the latter and the best-fitted metric $\log_{10} K$, respectively. Finally, the last two columns highlight the detectability of the metric used to generate the simulated data compared to all other metrics and compared to Schwarzschild only according to the BIC-based Bayes factor values.

The first main conclusion from Table 3 is that none of the metric signature can be clearly detected except the Boson star 2 model with GRAVITY uncertainties. However, except for the Gravastar 3 model (the most compact one), the fits of a hot spot in an ECO background are sufficiently better with ECO’s model

Background metric of data	best fitted metric	χ_{red}^2	BIC	2nd best fitted metric	$\log_{10} K$	detectable	exclude Sch
Schwarzschild	Schwarzschild ✓	0.94	60	Gravastar 1	1.1	~	
Boson star 2	Boson star 2 ✓	1.03	65	Fluid sphere 3	2.5	✓	✓
Boson star 3	Fluid sphere 2 ✗	0.71	50	Boson star 3	0.51	✗	✓
Fluid sphere 2	Fluid sphere 2 ✓	0.91	59	Boson star 3	0.56	✗	~
Fluid sphere 3	Fluid sphere 3 ✓	0.91	59	Boson star 3	0.28	✗	✓
Gravastar 1	Boson star 3 ✗	0.93	60	Gravastar 2	0.15	✗	✓
Gravastar 2	Gravastar 2 ✓	1.10	68	Gravastar 1	0.17	✗	✓
Gravastar 3	Schwarzschild ✗	1.00	64	Boson star 3	0.27	✗	✗

Table 3. Fit summary results for the studied metrics and Bayesian criteria: The first column lists the metric used for simulated data. The second column identifies the metric that best fits the data, alongside the reduced chi-squared (χ_{red}^2 , third column) and the Bayesian Information Criterion (BIC, fourth column). The fifth column reports the second best-fitting metric, and the sixth column shows the BIC-based Bayes factor. The seventh column indicates if the background metric is detectable per statistical criteria. The final column assesses the exclusion of the Schwarzschild metric based on statistical criteria. The uncertainties incorporated in the simulated data reflect GRAVITY’s typical uncertainties.

compared to Schwarzschild, so the latter can be excluded. This means that the impact of the plunge-through images into the polarization measurement is sufficiently important to exclude the Schwarzschild metric but not large enough (compared to the uncertainties) to distinguish one ECO metric from the other.

As mentioned above, the Boson star 2 metric is the only one that can be clearly detected. This is due to the large angular size of the plunge-through images in this model (see Rosa et al. 2025) which strongly affect the observed polarization fraction and Electric Vector Position Angle (EVPA). This can be seen in Fig. 6 which shows the contribution of the various images orders and nature, i.e. primary only in dotted line, primary + secondary (equivalent to Schwarzschild) in dashed line and all images including the plunge-through images in solid lines. The contribution of the plunge-through images is not constant with time and varies with the orbital phase creating the detectable signature.

Fig. 7 shows the best-fitted model in the Boson star 2 metric in solid lines and the best-fitted model in the Schwarzschild metric in dashed lines, with the simulated data generated in the Boson star 2 background. As expected, the astrometry in the Boson star 2 metric is shrunken compared to Schwarzschild due to the present of the plunge-through images; however, due to the large error bars, the constraint from the astrometric data points is lower than the polarimetric data points. We note that the two fits have found different values for the hot spot parameters. The fit in the Schwarzschild background compensates for the contribution from the plunge-through images with the hot spot parameters (mostly the linear polarization factor and the inclination). However, this compensation is not enough to properly fit the simulated data. The resulting χ_{red}^2 and BIC-based Bayes factor allow one to exclude the Schwarzschild metric.

Another interesting case is the fitting of simulated data made with the Boson star 3 background. The fit’s metric with the lowest χ_{red}^2 (Fluid sphere 2) does not correspond to the background metric of the simulated data. Moreover, χ_{red}^2 is significantly below 1 with a value of ~ 0.71 , indicating a possible overfit. Fig. 8 shows the comparison of the simulated data fits made with the Boson star 3 metric with the same metric in solid lines and with the best-fitted metric, the Fluid sphere 2 in dashed lines. Compared to Fig. 7, the two modeled curves (full and dashed lines) are more similar, with differences being of the same order (for polarization) or lower (for astrometry) than the uncertainties. This explains both the confusion of the correct metric type and the non-detection of the Boson star 3 metric.

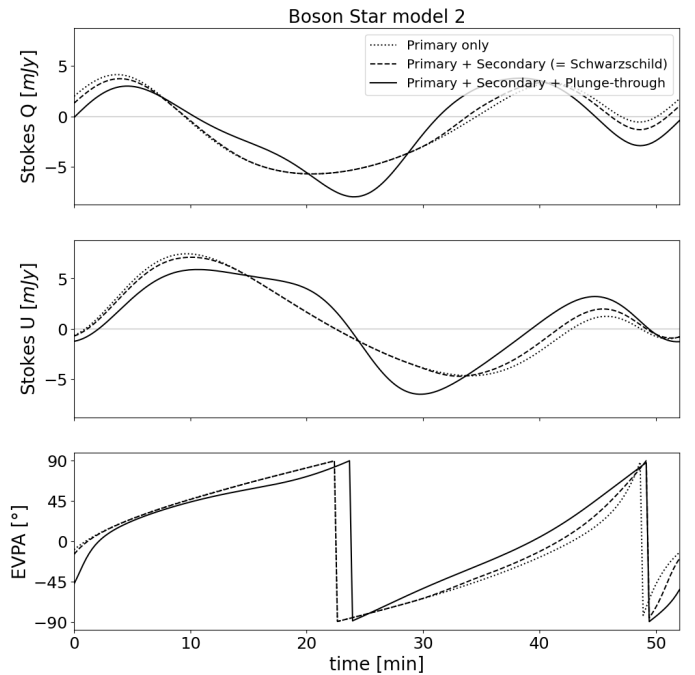


Fig. 6. Contribution of the various images orders and nature, i.e. primary only in dotted line, primary + secondary (equivalent to Schwarzschild) in dashed line and all images including the plunge-through images in solid lines.

The Gravastar models present significant challenges for detection. Specifically, the best metric derived from the fit does not align with the model that generated the data (as observed for simulated data in the Gravastar 1 and 3 models), or alternative Gravastar models produce qualitatively similar fittings, rendering them nearly indistinguishable (Gravastar 2 and Gravastar 1) with $\log_{10} K = 0.17 < 1$. To enhance the accuracy and detectability of these models, incorporating the radius of the Gravastar as a free, continuous parameter in the fitting process (an approach that exceeds the boundaries of this paper) rather than selecting discrete values could prove beneficial.

5.2. Future uncertainties with GRAVITY+/VLTI upgrades

In 2026, the upgrade of the GRAVITY instrument called GRAVITY+ should enter in service. This upgrade of the instrument it-

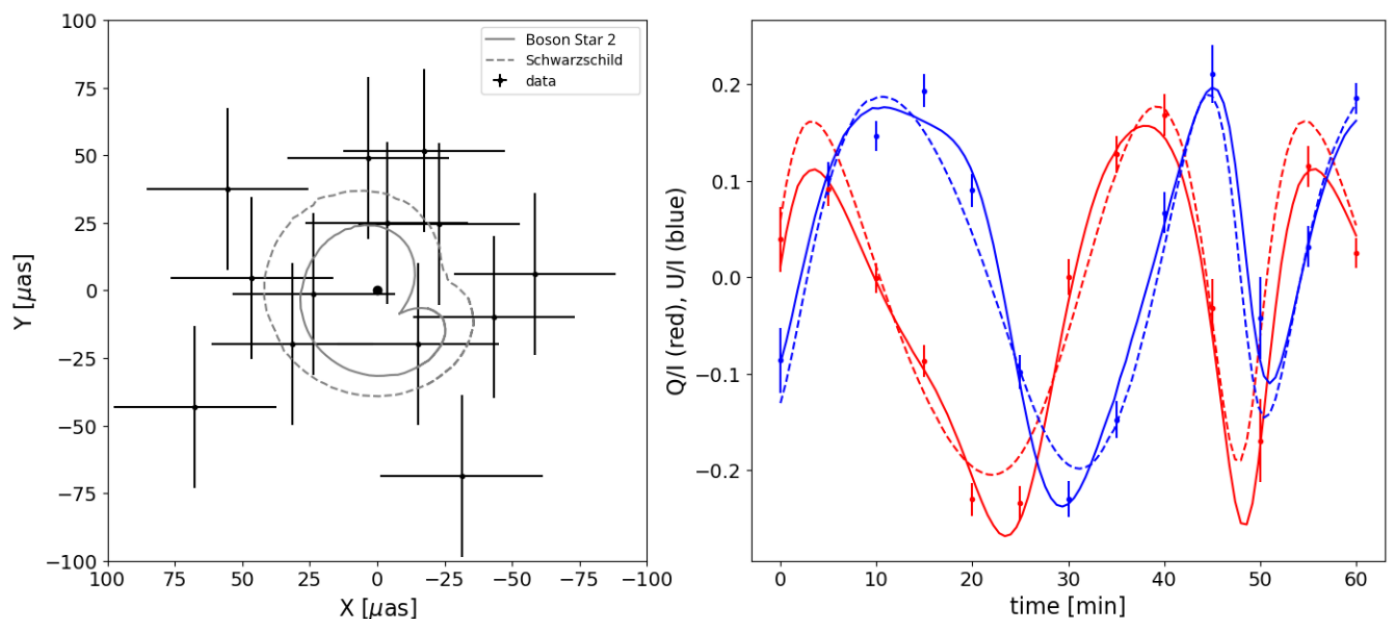


Fig. 7. Simulated data, generated in the Boson star 2 metric and represented by dots with error bars (reflecting GRAVITY-like uncertainties), are compared with two best-fitted models: one in the Boson star 2 metric (solid line) and one in the Schwarzschild metric (dashed lines). **Left-panel** shows the astrometry, and **right-panel** shows the time evolution of Q/I in red and U/I in blue.

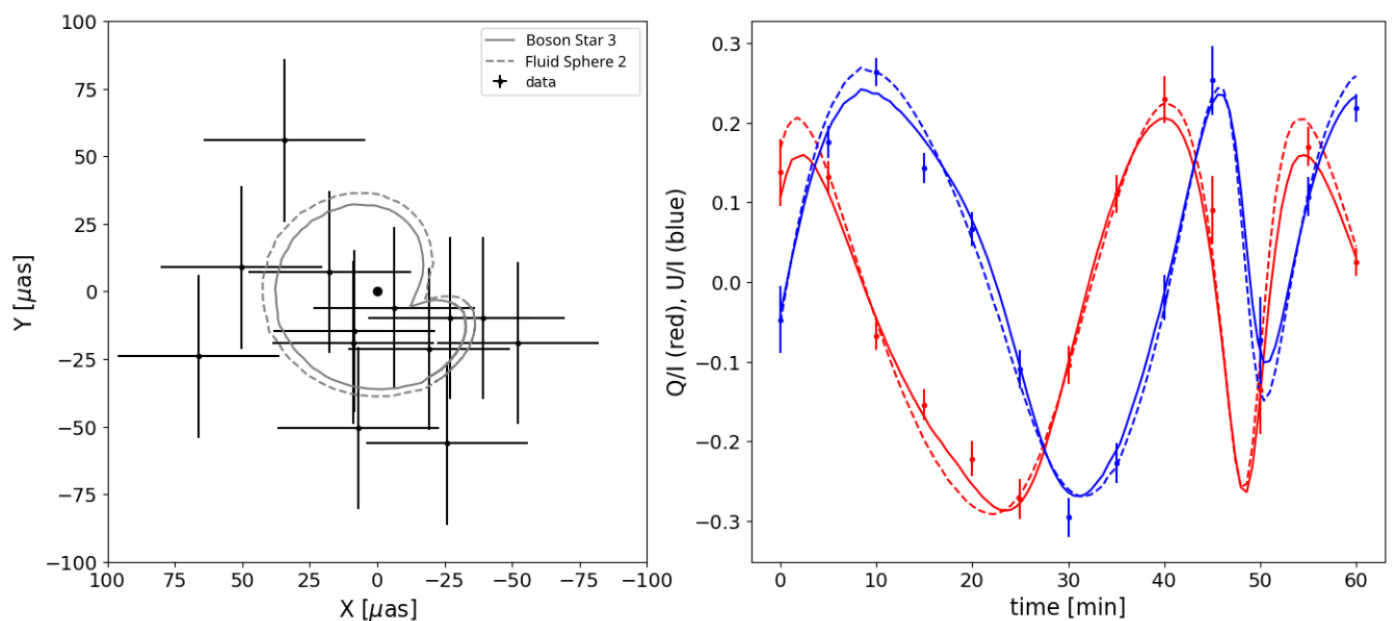


Fig. 8. Same as Fig. 7 with different simulated data that have been generated in the Boson star 3 metric, the best-fitted model also in the Boson star 3 metric (solid line) and the best-fitted model in the Fluid sphere 2 metric (dashed lines).

self also comes with an improvement of the VLTI infrastructure, including a better Adaptive Optic (AO) system with laser guide star on all Unit Telescope (UT; 8 meters telescopes) and better fringe tracking capabilities. The anticipated outcome of these enhancements is, optimally, an increase by a factor of 50 in the photon count within the fibers. This improvement can be interpreted as approximately a factor of $\sqrt{50} \sim 7$ in the signal-to-noise ratio with respect to flux uncertainties (Bourdarot & Eisenhauer 2024). Similarly, achieving the same level of flux uncertainties will be possible with a reduced integration time.

5.2.1. Smaller flux uncertainties

We therefore investigated how the optimal improvement on flux uncertainties affects the detectability of the studied ECO models. We performed the same analysis as in Sect. 5.1 with an uncertainty of the flux $\sigma_{\text{Flux}} = 0.03$ mJy (approximately seven times smaller than before). The results are listed in Table 4. Given the high level of photometric precision achieved, the influence of the plunge-through images, as induced by the various ECO models, exceeds the associated uncertainty. This leads to a considerably improved fit of the data when evaluated using the metric employed to generate the simulated data, as opposed to alternative metrics.

Background metric of data	best fitted metric	χ_{red}^2	BIC	2nd best fitted metric	$\log_{10} K$	detectable	exclude Sch
Schwarzschild	Schwarzschild ✓	1.03	65	Fluid sphere 2	54	✓	
Boson star 2	Boson star 2 ✓	0.95	62	Fluid sphere 3	210	✓	✓
Boson star 3	Boson star 3 ✓	1.12	70	Gravastar 2	12	✓	✓
Fluid sphere 2	Fluid sphere 2 ✓	1.38	82	Boson star 3	38	✓	✓
Fluid sphere 3	Fluid sphere 3 ✓	1.14	71	Gravastar 2	17	✓	✓
Gravastar 1	Gravastar 1 ✓	1.39	82	Gravastar 2	5.5	✓	✓
Gravastar 2	Gravastar 2 ✓	1.10	67	Gravastar 1	6.4	✓	✓
Gravastar 3	Gravastar 3 ✓	1.74	100	Fluid sphere 2	16	✓	✓

Table 4. Same as Table 3 with error bars on flux of 0.03 mJy (~ 7 times better compared to GRAVITY typical uncertainty which correspond to the improvement of sensitivity of GRAVITY+). We replace the column of K by $\log_{10} K$ as values reach extremely high numbers.

Similarly to Figs. 7 and 8, in Fig. 9 a comparison of the fits to the simulated data was made using the Gravastar 3 model, where $\sigma_{\text{Flux}} = 0.03$ mJy. The fits shown were made within the Gravastar 3 metric (represented by solid lines) and the Schwarzschild metric (depicted by dashed lines). At an early time (until $t \approx 30$ min), the polarimetric models in the Gravastar 3 and Schwarzschild metric are very close to each other, with differences lower than or of the same order as the (small) uncertainties. But this is no longer the case at later time, at $t \approx 50$ min (equivalent to an azimuthal angle of the hot spot of $\phi \approx 315^\circ$) where the difference between the two models is larger than the uncertainties resulting in a detectable signal.

We observe that the reduced chi-square, χ_{red}^2 , for fitting the dataset within the Fluid sphere 3 background using the identical metric is notably low, approximately 0.56, indicating potential overfitting.

5.2.2. Better time resolution

An alternative utilization of the GRAVITY+ and VLTI enhancements involves reducing the integration time from the standard 5-minute intervals to a more frequent 1-minute interval, while maintaining flux uncertainties comparable to those observed with the GRAVITY measurements. For observation of flares at the galactic center, such a scenario is more likely than the improvement of a factor seven on the flux uncertainties.

The impact of plunge-through images on polarization is not constant over time, suggesting that enhanced temporal resolution, achieved without compromising flux uncertainty, might be enough to differentiate between different metrics effectively. To evaluate this hypothesis, we have created simulated datasets, capturing one data point every minute, repeating the prior procedures to examine the results. The results of the fit analysis for each dataset are presented in Table 5. As expected, there is a noticeable enhancement in overall detectability, with nearly all metrics becoming at least partially detectable, with the exception of the Gravastar 2 metric. The latter remains too closely aligned with the Gravastar 1 metric. In line with earlier recommendations, when fitting actual data, the radius of the Gravastar metric should be considered as a continuous, adjustable parameter, rather than being restricted to three predetermined configurations. However, with this one-minute interval, the fits of all the data made in an ECO metric can exclude the Schwarzschild background even if the exact metric cannot be detected.

6. Limitations and discussion

6.1. Limitations

To verify the validity of our findings and ensure that they are not influenced by the specific simulated data used initially, we repeated the same analysis using some additional simulated data sets. These additional data sets were generated using the identical model setup and uncertainties σ_i . Due to the random effects from synthetic noise, the data points in these new datasets vary from their counterparts in the "initial" datasets. This variance affects the values of χ_{red}^2 , BIC , and AIC for the best fit, but does not significantly alter the relative values between the fits in different metrics. The BIC-based Bayes factor, representing the detectability level, can also vary. However, our conclusions remain the same, i.e., that with current uncertainties most metrics can not be detected but can be with better flux uncertainties as $\log_{10}(K) \gg 2$ for most of them.

In this study, we adopt a simplified hot-spot model characterized by uniform spatial parameters positioned along a circular orbit within the equatorial plane at the Schwarzschild keplerian velocity. This model is likely too rudimentary to adequately capture the flares of Sgr A* in NIR observations. The nature of motion, whether circular, helical, or conical, significantly influences both the observed astrometry Antonopoulou & Nathanail (2024) and the light curves (Aimar et al. 2023). Additionally, the orbital velocity, whether sub-Keplerian or super-Keplerian, has a substantial impact on the observables (Yfantis et al. 2024). The electron energy distribution (EED) is presumed to follow a Kappa distribution, with a constant power-law index at high energies, number density, and temperature, while variability is highly expected for flares. Indeed, acceleration mechanism by magnetic reconnection for example and synchrotron cooling play a crucial role for high-energy electrons and so flare modeling.

With a more sophisticated model, which includes more astrophysics (with its uncertainties), it is highly probable that the detectability of the metrics will decrease as the space-time characteristics could be diluted and degenerated with the astrophysical parameters. For example, a decrease of the polarization fraction as a result of the presence of plunge-through images can be partially mimicked by a rapid change in the intrinsic emission combined with the Shapiro effect (see Appendix B). This highlights the importance of accurate flare modeling.

Moreover, until now, we have not accounted for the quiescent state of Sgr A*. Although its impact is low when the flux from the flare is high, when the flux from the flare and the quiescent are comparable, i.e. at a later time, the quiescent might not be neglected.

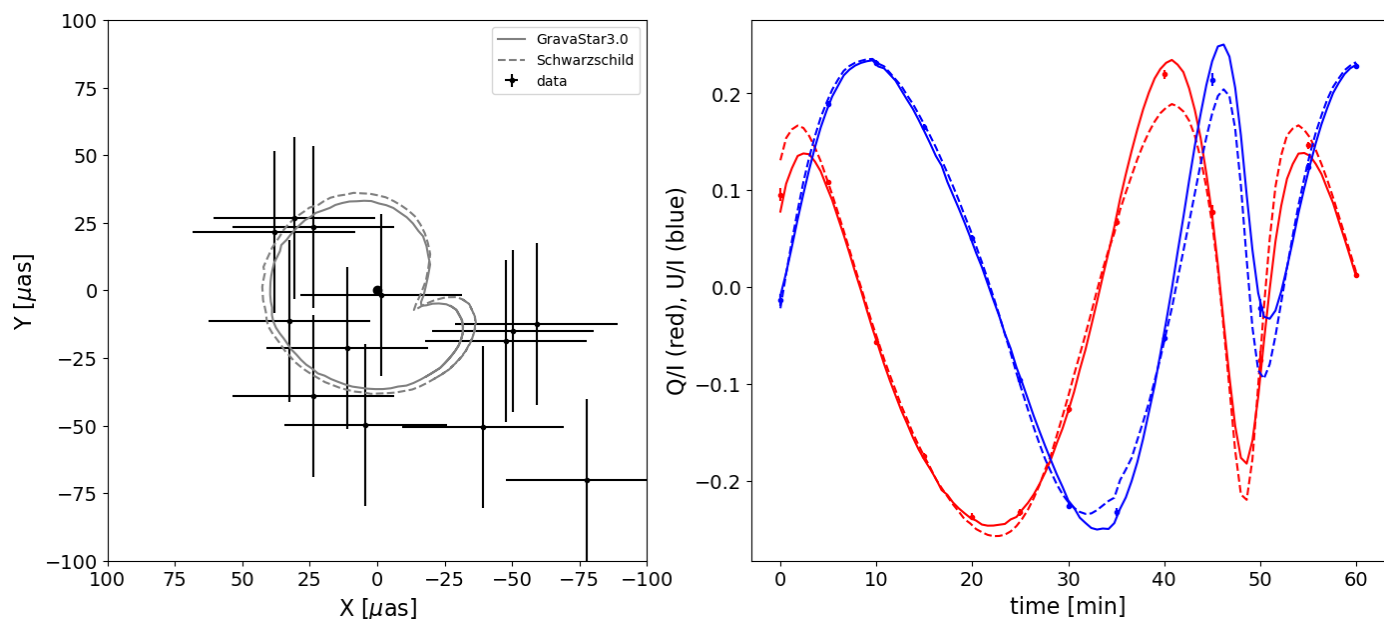


Fig. 9. Same as Fig. 7 with the simulated data being generated in the Gravastar 3 metric with flux uncertainties of $\sigma_{\text{Flux}} = 0.03$ mJy (anticipated GRAVITY+ precision), the best-fitted model also in the Gravastar 3 metric (solid line) and the best-fitted model in the Schwarzschild metric (dashed lines).

Background metric of data	best fitted metric	χ^2_{red}	BIC	2nd best fitted metric	$\log_{10} K$	detectable	exclude Sch
Schwarzschild	Schwarzschild ✓	0.95	249	Fluid sphere 2	5.2	✓	
Boson star 2	Boson star 2 ✓	0.99	260	Fluid sphere 3	23	✓	✓
Boson star 3	Boson star 3 ✓	1.08	281	Fluid sphere 2	1.1	~	✓
Fluid sphere 2	Fluid sphere 2 ✓	0.98	256	Gravastar 3	1.7	~	✓
Fluid sphere 3	Fluid sphere 3 ✓	1.10	287	Gravastar 2	2.7	✓	✓
Gravastar 1	Gravastar 1 ✓	0.90	238	Gravastar 2	2.4	✓	✓
Gravastar 2	Gravastar 2 ✓	0.88	233	Gravastar 1	0.43	✗	✓
Gravastar 3	Gravastar 3 ✓	0.89	235	Fluid sphere 2	2.9	✓	✓

Table 5. Similar to Table 3, but with enhanced temporal resolution, providing data at one-minute intervals.

6.2. Discussion

The encouraging results outlined in the previous discussion hold significant implications for the future observations planned with the advanced GRAVITY+ instrument and the upgraded Very Large Telescope Interferometer (VLTI). These advancements aim to detect the elusive ECO signatures in the flares emitted by Sagittarius A* (Sgr A*). Additionally, analogous polarization studies of Sgr A* flares have been conducted at radio frequencies, as detailed by Wielgus et al. (2022). At these wavelengths, considerations such as Faraday rotation and conversion effects cannot be disregarded, as the phenomena of accretion and ejection remain intensely luminous even during flare events. This scenario adds further complexity to the astrophysical processes observed in comparison to those in the near-infrared (NIR) spectrum. Despite these challenges, the exceptional temporal resolution provided by the Atacama Large Millimeter/submillimeter Array (ALMA) coupled with its remarkable ability to ascertain very low levels of polarized flux uncertainties renders this instrument an exceedingly promising candidate for the rigorous search for ECO signatures within the radio flares of Sgr A*.

The latest polarized images presented by Collaboration et al. (2024) provide a persuasive and distinct opportunity to ex-

plore the signatures of ECOs and to examine alternative gravitational theories (Yan 2024; Ahmed & Bouzenada 2024; Aliyan & Nozari 2024; Walia 2024; Vertogradov et al. 2025; Perrucci et al. 2025; Gan et al. 2024; Vishvakarma et al. 2025; Li et al. 2025).

Ultimately, with the improvements brought by the GRAVITY+ upgrade and the enhancements of the VLTI, alongside the anticipated new generation of NIR instruments integrated with the Extremely Large Telescope (ELT), it is anticipated that an increased number of stars will be discerned (Bourdarot & Eisenhauer 2024), with some being in close proximity to Sgr A*. This advance in observational capability will enable the conduction of further rigorous assessments of general relativity, the examination of ECO imprints on the trajectories of stellar bodies, as well as the evaluation of alternative gravitational theories. Such tests remain independent of the constraints posed by Sgr A* polarized flares, offering a complementary approach.

7. Summary and Conclusions

In this paper, we conducted an in-depth investigation into the detectability of space-time signatures through polarization measurements of individual flares from Sgr A*. For our analysis, we

employed an analytical model of a hot spot orbiting the compact object in its equatorial plane, specifically at the Schwarzschild keplerian velocity. Our examination encompassed a comprehensive set of eight different background metrics, derived from four distinct families of compact objects: Schwarzschild black holes, Boson stars, Fluid spheres, and Gravastars. These models included parameters for exotic compact objects crafted to mimic the behavior of regular black holes.

The principal distinction between the ECOs analyzed in this study and regular black holes lies in the existence of plunge-through images, which possess polarization properties comparable to the secondary image associated with the Schwarzschild space-time. These plunge-through images also contribute to an increased total intensity, thereby influencing both the observed Electric Vector Position Angle (EVPA) and the polarization fraction. Consequently, it becomes imperative to examine the normalized polarized quantities Q/I and U/I , rather than the original parameters Q and U .

To evaluate the detectability of a specified metric, we generated simulated data corresponding to this metric and executed 8 fits (one for each metric under investigation). The metric with the lowest χ_{red}^2 is considered to be the best-fitted metric. To state whether a metric is detectable or not, we compare the BIC-based Bayes factor K between the best-fitted metric and the other metrics. If the smallest difference $\log_{10} K$ is greater than 2, we consider that the best fit is sufficiently better than the other to state that it is detectable; otherwise, it is not.

The imprints on polarization measurements from the plunge-through images are of the same order as the current measurement uncertainties associated with the GRAVITY instrument. As a result, distinguishing between these metrics is feasible unambiguously (refer to Table 3), only for the Boson star 2 model. Nevertheless, even with the current uncertainties, the Schwarzschild fits of simulated data made in an ECO metric are sufficiently worse that we can exclude the Schwarzschild metric. We also made prediction of the detectability of ECOs with the upcoming upgrade of the GRAVITY instrument: GRAVITY+. With a ~ 7 times small flux uncertainties or a higher time resolution than we can expect with this upgrade, all metrics are detectable unambiguously (see Tables 4 and 5).

However, the model used in this study is very simplistic, with very little astrophysics (only the vertical magnetic field configuration from Gravity Collaboration et al. (2023) and synchrotron emission). Most of the photometric properties are governed by relativistic effects like beaming, Doppler Boosting, and light bending. In reality, flares are much more complex with a lot of astrophysical uncertainties that mitigate detectability and can lead to an incorrect best-fit metric.

Nevertheless, this advancement opens up a realm of exciting opportunities and holds substantial promise for the future of astronomical observations, paving the way for innovative discoveries and pushing the boundaries of our understanding of the universe.

Acknowledgements. N.A and P.G. acknowledge the Fundação para a Ciência e a Tecnologia (FCT), Portugal, for the financial support to the Center for Astrophysics and Gravitation—CENTRA, Instituto Superior Técnico, Universidade de Lisboa, through Project No. UIDB/00099/2020. The authors thankfully acknowledge the computer resources, technical expertise and assistance provided by CENTRA/IST. Computations were performed at the cluster “Baltasar-Sete-Sóis” and supported by the H2020 ERC Consolidator Grant “Matter and strong field gravity: New frontiers in Einstein’s theory” grant agreement no. MaGRaTh-646597. The authors thank Saurabh, Thibaut Paumard and Frédéric Vincent for fruitful discussions.

References

- Ahmed, F. & Bouzenada, A. 2024, *European Physical Journal C*, 84, 1271
- Aimar, N., Dmytriiev, A., Vincent, F. H., et al. 2023, *A&A*, 672, A62
- Aimar, N., Paumard, T., Vincent, F. H., Gourgoulhon, E., & Perrin, G. 2024, *Classical and Quantum Gravity*, 41, 095010
- Aliyan, F. & Nozari, K. 2024, *Physics of the Dark Universe*, 46, 101611
- Antonopoulou, E. & Nathanail, A. 2024, arXiv e-prints, arXiv:2405.10115
- Baganoff, F. K., Bautz, M. W., Brandt, W. N., et al. 2001, *Nature*, 413, 45
- Barrière, N. M., Tomsick, J. A., Baganoff, F. K., et al. 2014, *ApJ*, 786, 46
- Bourdarot, G. & Eisenhauer, F. 2024, arXiv e-prints, arXiv:2410.22063
- Bower, G. C., Markoff, S., Dexter, J., et al. 2015, *ApJ*, 802, 69
- Brinkerink, C. D., Falcke, H., Law, C. J., et al. 2015, *A&A*, 576, A41
- Broderick, A. E. & Loeb, A. 2006, *MNRAS*, 367, 905
- Carballo-Rubio, R., Di Filippo, F., & Liberati, S. 2022, *Physical Review D*, 106, 124048
- Cardoso, V. & Pani, P. 2019, *Living Reviews in Relativity*, 22, 4
- Collaboration, T. E. H. T., Akiyama, K., Alberdi, A., et al. 2024, *The Astrophysical Journal Letters*, 964, L25
- De Laurentis, M., de Martino, I., & Della Monica, R. 2023, *Reports on Progress in Physics*, 86, 104901
- Do, T., Ghez, A. M., Morris, M. R., et al. 2009, *ApJ*, 691, 1021
- Doe, J. & Others. 2024, ArXiv e-prints [arXiv:2408.09893]
- Event Horizon Telescope Collaboration, Akiyama, K., Alberdi, A., et al. 2024, *ApJ*, 964, L26
- Event Horizon Telescope Collaboration, Akiyama, K., Alberdi, A., et al. 2022, *ApJ*, 930, L12
- Foschi, A., Abuter, R., Aimar, N., et al. 2023, *MNRAS*, 524, 1075
- Gan, X., Wang, L.-T., & Xiao, H. 2024, *Phys. Rev. D*, 110, 063039
- Genzel, R., Schödel, R., Ott, T., et al. 2003, *Nature*, 425, 934
- Ghez, A. M., Wright, S. A., Matthews, K., et al. 2004, *ApJ*, 601, L159
- Gillessen, S., Plewa, P. M., Eisenhauer, F., et al. 2017, *ApJ*, 837, 30
- GRAVITY Collaboration, Abuter, R., Accardo, M., et al. 2017, *A&A*, 602, A94
- Gravity Collaboration, Abuter, R., Aimar, N., et al. 2023, *A&A*, 677, L10
- GRAVITY Collaboration, Abuter, R., Aimar, N., et al. 2022, *A&A*, 657, L12
- GRAVITY Collaboration, Abuter, R., Amorim, A., et al. 2018a, *A&A*, 615, L15
- GRAVITY Collaboration, Abuter, R., Amorim, A., et al. 2021, *A&A*, 654, A22
- GRAVITY Collaboration, Abuter, R., Amorim, A., et al. 2020, *A&A*, 636, L5
- GRAVITY Collaboration, Abuter, R., Amorim, A., et al. 2018b, *A&A*, 618, L10
- GRAVITY Collaboration, Foschi, A., Abuter, R., et al. 2024, *MNRAS*, 530, 3740
- Haggard, D., Nynka, M., Mon, B., et al. 2019, *ApJ*, 886, 96
- Hamaus, N., Paumard, T., Müller, T., et al. 2009, *ApJ*, 692, 902
- Hawking, S. W. 1976, *Phys. Rev. D*, 14, 2460
- Hora, J. L., Witzel, G., Ashby, M. L. N., et al. 2014, *ApJ*, 793, 120
- Hornstein, S. D., Matthews, K., Ghez, A. M., et al. 2007, *ApJ*, 667, 900
- Kass, R. E. & and, A. E. R. 1995, *Journal of the American Statistical Association*, 90, 773
- Li, G.-P., Wu, M.-Q., He, K.-J., & Jiang, Q.-Q. 2025, arXiv e-prints, arXiv:2505.14734
- Li, Z. & Bambi, C. 2014, *Phys. Rev. D*, 90, 024071
- Li, Z., Kong, L., & Bambi, C. 2014, *ApJ*, 787, 152
- Lin, X., Li, Y.-P., & Yuan, F. 2023, *MNRAS*, 520, 1271
- Liu, D., Li, Z., & Bambi, C. 2015, *J. Cosmology Astropart. Phys.*, 2015, 020
- Marszewski, A., Prather, B. S., Joshi, A. V., Pandya, A., & Gammie, C. F. 2021, *ApJ*, 921, 17
- Nayakshin, S., Cuadra, J., & Sunyaev, R. 2004, *A&A*, 413, 173
- Neilsen, J., Nowak, M. A., Gammie, C., et al. 2013, *ApJ*, 774, 42
- Nowak, M. A., Neilsen, J., Markoff, S. B., et al. 2012, *ApJ*, 759, 95
- Penrose, R. 1965, *Phys. Rev. Lett.*, 14, 57
- Penrose, R. 1969, *Nuovo Cimento Rivista Serie*, 1, 252
- Perrucci, I., Kuipers, F., & Casadio, R. 2025, *J. Cosmology Astropart. Phys.*, 2025, 005
- Ponti, G., De Marco, B., Morris, M. R., et al. 2015, *MNRAS*, 454, 1525
- Rosa, J. a. L., Aimar, N., & Liis Tamm, H. 2025, arXiv e-prints, arXiv:2504.02472
- Rosa, J. a. L., Cordeiro, D. S. J., Macedo, C. F. B., & Lobo, F. S. N. 2024, *Phys. Rev. D*, 109, 084002
- Rosa, J. a. L., Macedo, C. F. B., & Rubiera-Garcia, D. 2023, *Phys. Rev. D*, 108, 044021
- Rosa, J. L., Garcia, P., Vincent, F. H., & Cardoso, V. 2022, *Phys. Rev. D*, 106, 044031
- Shaikh, R. 2022, *Monthly Notices of the Royal Astronomical Society*, 517, 1967
- Tagger, M. & Melia, F. 2006, *ApJ*, 636, L33
- Tamm, H. L. & Rosa, J. a. L. 2024, *Phys. Rev. D*, 109, 044062
- The GRAVITY Collaboration, El Dayem, K. A., Abuter, R., et al. 2025, arXiv e-prints, arXiv:2504.02908
- Vagnozzi, S., Visinelli, L., & Others. 2022, *Classical and Quantum Gravity*, 40, 165007
- Vertogradov, V., Misyura, M., & Bambhaniya, P. 2025, *European Physical Journal Plus*, 140, 23

- Vincent, F. H., Paumard, T., Gourgoulhon, E., & Perrin, G. 2011, *Classical and Quantum Gravity*, 28, 225011
- Vincent, F. H., Paumard, T., Perrin, G., et al. 2014, *MNRAS*, 441, 3477
- Vincent, F. H., Wielgus, M., Aimar, N., Paumard, T., & Perrin, G. 2024, *A&A*, 684, A194
- Vishvakarma, B. K., Kala, S., & Siwach, S. 2025, *Annals of Physics*, 475, 169957
- von Fellenberg, S. D., Roychowdhury, T., Michail, J. M., et al. 2025, *ApJ*, 979, L20
- Wagenmakers, E.-J. 2007, *Psychonomic Bulletin & Review*, 14, 779
- Walia, R. K. 2024, *Phys. Rev. D*, 110, 064058
- Wielgus, M., Mościbrodzka, M., Vos, J., et al. 2022, *A&A*, 665, L6
- Yan, Z. 2024, arXiv e-prints, arXiv:2412.20109
- Yfantis, A. I., Wielgus, M., & Mościbrodzka, M. A. 2024, arXiv e-prints, arXiv:2408.07120
- Yusef-Zadeh, F., Roberts, D., Wardle, M., Heinke, C. O., & Bower, G. C. 2006, *ApJ*, 650, 189

Appendix A: "Blind" tests results

To ensure the accuracy of our findings and verify that they do not rely on a particular selection of values, we have conducted two "blind" tests. In these tests, the parameters, including the background metric, remain unknown to the individual conducting the analysis. This approach effectively reduces any potential biases or preconceived notions that might influence the fitting process and its outcomes.

These tests involved the use of simulated data sets and, notably, these datasets were generated by individuals other than the one performing the data fitting analysis. Details concerning the parameters used to generate these simulated datasets, including the specific metric used, together with the resulting best-fit parameters, are reported in Table A.1. We used the GRAVITY uncertainties for these tests. For the first blind dataset, which has been generated in the Gravastar 2 metric, we found the correct metric (and correct parameter estimation) as earlier, but the BIC-based Bayes factor is too low ($\min(\log_{10} K) = 0.17$) to claim a detection (as before). For the second data set, which has been generated in the Fluid sphere 3 metric, we did not find the correct metric (it is the second-best metric) as the best-fitted metric is the Gravastar 1. We note that the estimated values of the parameters are a bit offset from the "real" values (especially φ_0). The BIC-based Bayes factor is again too low to distinguish the first and second-best fit metric ($\log_{10} K = 0.47$). However, in both cases, the Schwarzschild metric can be excluded. We thus obtained very similar results to those in Sect. 5.1 validating our results.

Appendix B: Impact of inadequate flare model

To assess the impact of inadequate flare modeling on the presented results, we performed the same analysis using simulated data generated with a model that incorporates intrinsic time variability (Gaussian time modulation) with minor flux uncertainties ($\sigma_{\text{Flux}} = 0.03\text{mJy}$). The findings are summarized in Table B.1. In certain instances, intrinsic variability causes a discrepancy between the "true" data metric and the best-fit metric. Notably, for some cases (such as Boson star 3 and Gravastar 2), this variability reduces the BIC-based Bayes factor to the point that detection is no longer possible, preventing any conclusions about the data's metric. In contrast, there are situations where the best-fit metric does not align with the data metric, yet the BIC-based Bayes factor remains sufficiently high for detection, potentially leading to an entirely erroneous conclusion, with the only indication being a high χ_{red}^2 .

Parameter	Symbol	Blind Test 1	Best-fit	Blind Test 2	Best-fit
Orbital radius [r_g]	r	10	10.07 ± 0.07	11	10.68 ± 0.05
Azimuthal angle at $t^{BL} = 0$ [$^\circ$]	φ_0	180	180.52 ± 1.1	5	0.51 ± 0.39
Inclination [$^\circ$]	i	160	159.51 ± 0.35	148.1	146.93 ± 0.26
Linear polarization factor	lp	0.7	0.72 ± 0.02	0.87	0.85 ± 0.01
metric		Gravastar 2	Gravastar 2	Fluid sphere 3	Gravastar 1

Table A.1. Summary of the parameters of the hot-spot model used to generate the simulated data for the blind tests and the fitted values.

Background metric of data	best fitted metric	χ_{red}^2	BIC	2nd best fitted metric	$\log_{10} K$	detectable	exclude Sch
Schwarzschild	Schwarzschild ✓	2.25	124	Gravastar 1	18	✓	
Boson star 2	Boson star 2 ✓	12.63	622	Fluid sphere 3	62	✓	✓
Boson star 3	Gravastar 1 ✗	6.85	344	Boson star 3	0.81	✗	✓
Fluid sphere 2	Fluid sphere 2 ✓	5.81	294	Schwarzschild	2.4	✓	✓
Fluid sphere 3	Gravastar 2 ✗	6.98	351	Fluid sphere 3	0.97	✗	✓
Gravastar 1	Gravastar 1 ✓	4.17	216	Gravastar 2	6.9	✓	✓
Gravastar 2	Gravastar 1 ✗	5.71	290	Gravastar 2	5.3	✓	✓
Gravastar 3	Schwarzschild ✗	5.79	294	Gravastar 3	14	✓	

Table B.1. Same as Table 4 with simulated data generated with a Gaussian time modulation.